AGU PUBLICATIONS

JGR

Journal of Geophysical Research: Solid Earth

RESEARCH ARTICLE
10.1002/2015JB012783

Key Points:
- Documenting the first magnetic profiles in fast-spreading lower crust and upper mantle
- Magnetically detect lithological contacts in fast-spreading lower crust and shallow mantle
- Developing the vertical magnetic profiling approach for the first time in 3-D

Supporting Information:
- Supporting Information S1

Correspondence to:
M. Tominaga,
masako.tominaga@tamu.edu

Citation:
Tominaga, M., M. A. Tivey, C. J. MacLeod, A. Morris, C. J. Lissenberg, D. J. Shillington, and V. Ferrini (2016), Characterization of the in situ magnetic architecture of oceanic crust (Hess Deep) using near-source vector magnetic data, *J. Geophys. Res. Solid Earth*, *121*, 4130–4146, doi:10.1002/2015JB012783.

Received 4 JAN 2016
Accepted 16 MAY 2016
Accepted article online 19 MAY 2016
Published online 16 JUN 2016

Characterization of the in situ magnetic architecture of oceanic crust (Hess Deep) using near-source vector magnetic data

Masako Tominaga[1], Maurice A. Tivey[2], Christopher J. MacLeod[3], Antony Morris[4], C. Johan Lissenberg[3], Donna J. Shillington[5], and Vicki Ferrini[5]

[1]Department of Geology and Geophysics, Texas A&M University, College Station, Texas, USA, [2]Department of Geology and Geophysics, Woods Hole Oceanographic Institution, Falmouth, Massachusetts, USA, [3]School of Earth and Ocean Sciences, Cardiff University, Cardiff, UK, [4]School of Geography, Earth, and Environmental Sciences, University of Plymouth, Plymouth, UK, [5]Lamont-Doherty Earth Observatory, Columbia University, Palisades, New York, USA

Abstract Marine magnetic anomalies are a powerful tool for detecting geomagnetic polarity reversals, lithological boundaries, topographic contrasts, and alteration fronts in the oceanic lithosphere. Our aim here is to detect lithological contacts in fast-spreading lower crust and shallow mantle by characterizing magnetic anomalies and investigating their origins. We conducted a high-resolution, near-bottom, vector magnetic survey of crust exposed in the Hess Deep "tectonic window" using the remotely operated vehicle (ROV) *Isis* during RRS *James Cook* cruise JC21 in 2008. Hess Deep is located at the western tip of the propagating rift of the Cocos-Nazca plate boundary near the East Pacific Rise (EPR) (2°15'N, 101°30'W). ROV *Isis* collected high-resolution bathymetry and near-bottom magnetic data as well as seafloor samples to determine the in situ lithostratigraphy and internal structure of a section of EPR lower crust and mantle exposed on the steep (~20°dipping) south facing slope just north of the Hess Deep nadir. Ten magnetic profiles were collected up the slope using a three-axis fluxgate magnetometer mounted on ROV *Isis*. We develop and extend the vertical magnetic profile (VMP) approach of Tivey (1996) by incorporating, for the first time, a three-dimensional vector analysis, leading to what we here termed as "vector vertical magnetic profiling" approach. We calculate the source magnetization distribution, the deviation from two dimensionality, and the strike of magnetic boundaries using both the total field Fourier-transform inversion approach and a modified differential vector magnetic analysis. Overall, coherent, long-wavelength total field anomalies are present with a strong magnetization contrast between the upper and lower parts of the slope. The total field anomalies indicate a coherently magnetized source at depth. The upper part of the slope is weakly magnetized and magnetic structure follows the underlying slope morphology, including a "bench" and lobe-shaped steps, imaged by microbathymetry. The lower part of the slope is strongly magnetized, with a gradual reduction in amplitude from east to west across the slope. Surface morphology and recent drilling results indicate that the slope has been affected by mass wasting, but the observation of internally coherent magnetization distributions within the upper and lower slopes suggest that the disturbance is surficial. We attribute the spatial differences in magnetization distribution to the combination of changes in in situ lithology and depth to the source. These survey lines document the first magnetic profiles that capture the gabbro-ultramafic and possibly dike-gabbro boundaries in fast-spreading lower crust.

1. Introduction

In "normal spreading" environments with a "Penrose-type" "layer cake" upper crustal sequence [*Anonymous*, 1972], the dominant source of marine magnetic anomalies is thought to be the extrusive basaltic layer [e.g., *Harrison*, 1987]. The coherency in aligned magnetic anomalies recorded within this basaltic crust—the magnetic stripes—is fundamental evidence underpinning the seafloor spreading hypothesis [*Vine and Matthews*, 1963]. Studies of lower crustal gabbros and upper mantle peridotites suggest that these deeper lithologies are also capable of contributing to the marine magnetic anomaly signal [e.g., *Fox and Opdyke*, 1973; *Kidd*, 1977; *Arkani-Hamed*, 1988; *Pariso and Johnson*, 1993; *Johnson and Pariso*, 1993; *Gee and Kent*, 2007].

It is now recognized that large areas of ocean crust formed at slow spreading spreading centers are nonbasaltic at the seafloor [*Escartin et al.*, 2008; *Smith et al.*, 2006, 2008]. Lower crustal and upper mantle rocks are exposed via low-angle detachment faults associated with oceanic core complexes (OCCs) [e.g., Kane Megamullion:

Tucholke et al., 1998; *Dick et al.*, 2008; Atlantis Bank: *Dick et al.*, 2000; *Allerton and Tivey*, 2001; 15°N core complexes: *MacLeod et al.*, 2002; *Fujiwara et al.*, 2003; 13°N: *Smith et al.*, 2006, 2008; *MacLeod et al.*, 2009; Logatchev Massif: *Garcés and Gee*, 2007; Atlantis Massif: *Morris et al.*, 2009; *Zhao and Tominaga*, 2009]; and by rift basins [e.g., Iberia/Newfoundland margins, *Russell and Whitmarsh*, 2003; Endeavor Deep: *Richmond et al.*, 2004]. Magnetic anomalies are present in areas that lack a basaltic carapace, implying the presence of a magnetized lower crust and upper mantle [*Allerton and Tivey*, 2001; *Baines et al.*, 2008]. The coherency of these magnetic anomalies is not always evident in these OCC environments, however, presumably due to episodic magmatic emplacement and time-lagged magnetization acquisition and alteration processes in the exposed gabbro and serpentinized peridotite [e.g., *Tivey and Tucholke*, 1998; *Tominaga and Sager*, 2010; *Mallows and Searle*, 2012]. This absence or presence of coherency in observed magnetic anomalies can provide important information on the lithological variations within a magnetic source layer, its geometry, and the kinematic history, as well as the possible timing of magnetization [e.g., *Allerton and Tivey*, 2001]. In fast-spreading environments, however, although a contribution from the lower crustal section to seafloor spreading magnetic anomalies has been suggested, it has been viewed as subordinate [*Kikawa and Ozawa*, 1992] to the strongly magnetized and thinner (0.5–1 km) basaltic extrusive layer. Indeed, while magmatic lower crustal emplacement processes may be more continuous over time compared to slow spreading ridges, the magnetization polarity structure in fast-spreading lower crust likely follows shallow dipping Curie temperature isotherms that only impart longer wavelength contributions to the magnetic anomaly structure [*Kidd*, 1977; *Wilson and Hey*, 1981; *Phipps Morgan and Chen*, 1993].

Most published marine magnetic studies to date only use total magnetic field anomaly data. The development of vector magnetic data analyses with directional information (x, y, and z components with respect to geomagnetic north) offers the opportunity to provide additional insight into the magnetic crustal structure [e.g., *Isezaki*, 1986; *Seama et al.*, 1993; *Korenaga*, 1995; *Lee and Kim*, 2004]. High-precision vector magnetometers mounted on human-occupied submersibles, remotely operated vehicles (ROVs) or autonomous underwater vehicles provide unprecedented data resolution and make it possible to directly relate magnetic anomalies with subsurface geological processes on the outcrop scale [e.g., *Honsho et al.*, 2012; *Tivey et al.*, 2014; *Szitkar et al.*, 2015].

In this study, we present near-bottom three-axis vector magnetic data from the south facing slope of Hess Deep, where gabbroic lower crustal and serpentinized peridotitic upper mantle rocks from the East Pacific Rise (EPR) are exposed at the seafloor [*Francheteau et al.*, 1990; *Gillis et al.*, 1993; *Lissenberg et al.*, 2013]. Our goal is to investigate the magnetic character of lower crust and upper mantle material and to derive the implications of this magnetism for the structure and composition of the south facing slope of Hess Deep, the site of the currently active rift valley system of Hess Deep. Due to the sloping nature of the terrain, we develop and extend the vertical magnetic profiling (VMP) approach of *Tivey* [1996] by incorporating a three-dimensional vector analysis for the first time—what we term here as a "vector vertical magnetic profiling" approach (hereinafter referred to as Vector-VMP or VVMP).

2. Background

2.1. Hess Deep Rift Valley

Hess Deep rift valley (2°N, 101°W) is located near the western tip of the westward propagating Cocos-Nazca spreading center at the northern margin of the Galapagos microplate [*Raff*, 1968; *Johnson et al.*, 1976; *Hey*, 1977; *Schouten et al.*, 2008; *Smith et al.*, 2013] (Figures 1a and 1b). The Cocos-Nazca spreading center is propagating westward at a rate similar to the 66.5 mm/yr half-spreading rate of the adjacent EPR [*Lonsdale*, 1988; *DeMets et al.*, 2010; *Rioux et al.*, 2012]. Young lithosphere formed at the EPR is currently being rifted by the Cocos-Nazca spreading center [*Lonsdale*, 1988]. The western tip of the Hess Deep rift is composed of the Hess Deep valley (5400 m deep), an intrarift ridge just to the north, and the tip of the intermediate-spreading Cocos-Nazca spreading center just to the east (Figures 1a and 1b).

The formation history of the Hess Deep region has been investigated by submersible studies [*Francheteau et al.*, 1990; *Karson et al.*, 1992] and drilling [*Gillis et al.*, 1993, 2014] (Figures 1b and 2). *Francheteau et al.* [1990] documented outcrops of the intrarift ridge and Nazca-Cocos spreading center in the Hess Deep rift valley through dredging and submersible dives. The north wall of Hess Deep has been investigated by submersible *Alvin* [*Karson et al.*, 1992]. Vertical transects of this north wall reveal a crustal stratigraphy of

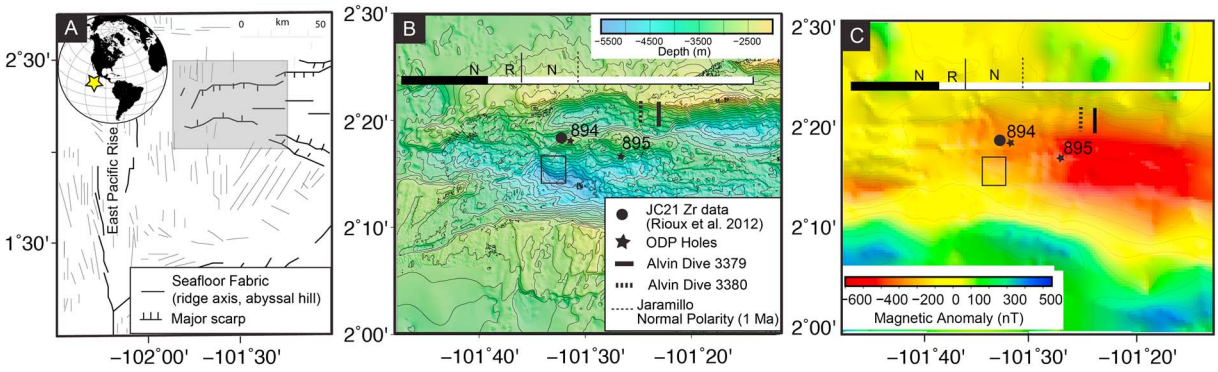

Figure 1. (a) Map of the East Pacific Rise with a line drawing of the major seafloor fabric trends in the Hess Deep region. The inset globe shows the location of the Hess Deep rift valley in the global context. (b) Bathymetry map of Hess Deep rift valley based on the new JC21 shipboard multibeam data. (c) Compilation of observed sea surface magnetic anomalies, including the JC21 data. Previous drilled sites (Sites 894 and 895) [*Gillis et al.*, 1993] and Alvin dive sites (3379 and 3380; e.g., *Karson et al.*, 1992] are indicated. The gray box indicates the area shown in Figures 1b and 1c. The square shows the location of the survey area on the south facing slope. The polarity bar (black: normal, white: reverse) is placed to indicate the polarity distribution of the adjacent EPR crust. The polarity boundaries and the combination of thin solid and dotted lines are extrapolated from magnetic anomalies observed at 3°N and 1°N over East Pacific Rise seafloor where little disturbance of the anomalies due to the Galapagos Microplate and Hess Deep rift valley is observed. The older end, the dotted lines indicate 1.0 Ma crustal isochron, i.e., the old end of the Jaramillo Normal Polarity.

the exposed portion of the EPR lithosphere of an extrusive basaltic layer, the sheeted dike complex, and minor outcrops of uppermost gabbros. Ocean Drilling Program (ODP) Leg 147 drilled: (i) a 150 m deep hole into gabbros on the western summit of the intrarift ridge (Hole 894G) and (ii) two ~100 m holes (at Site 895) into harzburgites and dunites on the southern flank of the eastern end of the intrarift ridge, which is inferred to be a crust-mantle transition zone [*Gillis et al.*, 1993] (Figure 2). Based on early tectonic mapping and submersible sampling [*Francheteau et al.*, 1990], paleomagnetic and rock magnetic analyses [*Hurst et al.*, 1994; *Varga et al.*, 2004], and a tectonic synthesis of the Leg 147 results [*MacLeod et al.*, 1996], two different models for the formation of intrarift ridge and Hess Deep valley were developed. One model suggests that the intrarift ridge is the result of uplift by serpentinite diapirism [*Francheteau et al.*, 1990] and the other model suggests it is a horst lying above a south-dipping, low-angle detachment fault [*MacLeod et al.*, 1996].

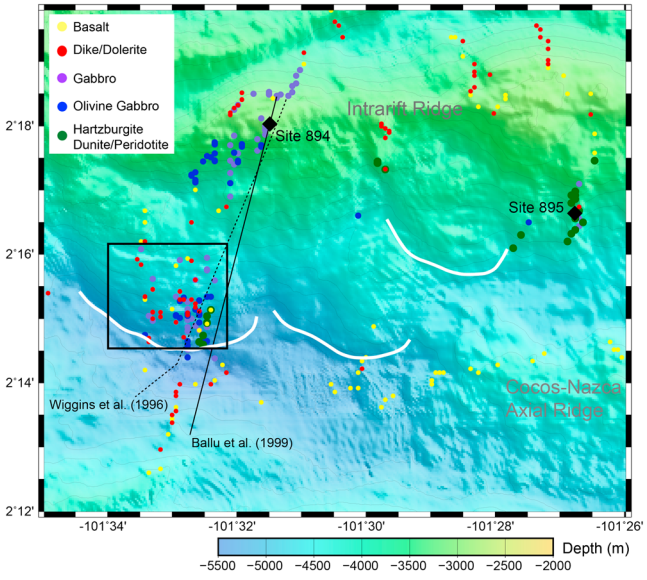

Figure 2. A summary of the previous studies overlying the new JC21 shipboard bathymetry data based on *Francheteau et al.* [1990], *Gillis et al.* [1993], *Wiggins et al.* [1996], and *Ballu et al.* [1999]. Lithologies are based on a compilation of previous sampling dives and JC21 results [*MacLeod et al.*, 2008]. The dotted and solid lines indicate seismic and gravity experiment profiles by *Ballu et al.* [1999] and *Wiggins et al.* [1996], respectively. White lines trace the large-scale tectonic sole of slipped blocks in the vicinity of Hess Deep. The black square indicates the survey site (Figure 3).

During the recent Integrated Ocean Drilling Program (IODP) Expedition 345, Site U1415 drilled and recovered core samples of the lower half to one third of the EPR plutonic crust, providing the first reference section for primitive fast-spreading oceanic lower crust (Figure 3) [*Gillis et al.*, 2014]. Magnetic orientations observed in the core samples suggest that the drilled section of Site U1415 consists of a series of blocks with various (a few tens of meters) thicknesses and block rotations formed by mass wasting [*Gillis et al.*, 2014]: (a) data from IODP Hole U1415J have positive inclinations (of approximately +30°) in the top 40 m below seafloor (mbsf) overlying a zone from 40 to 100 mbsf with negative inclinations (of approximately −45°) but

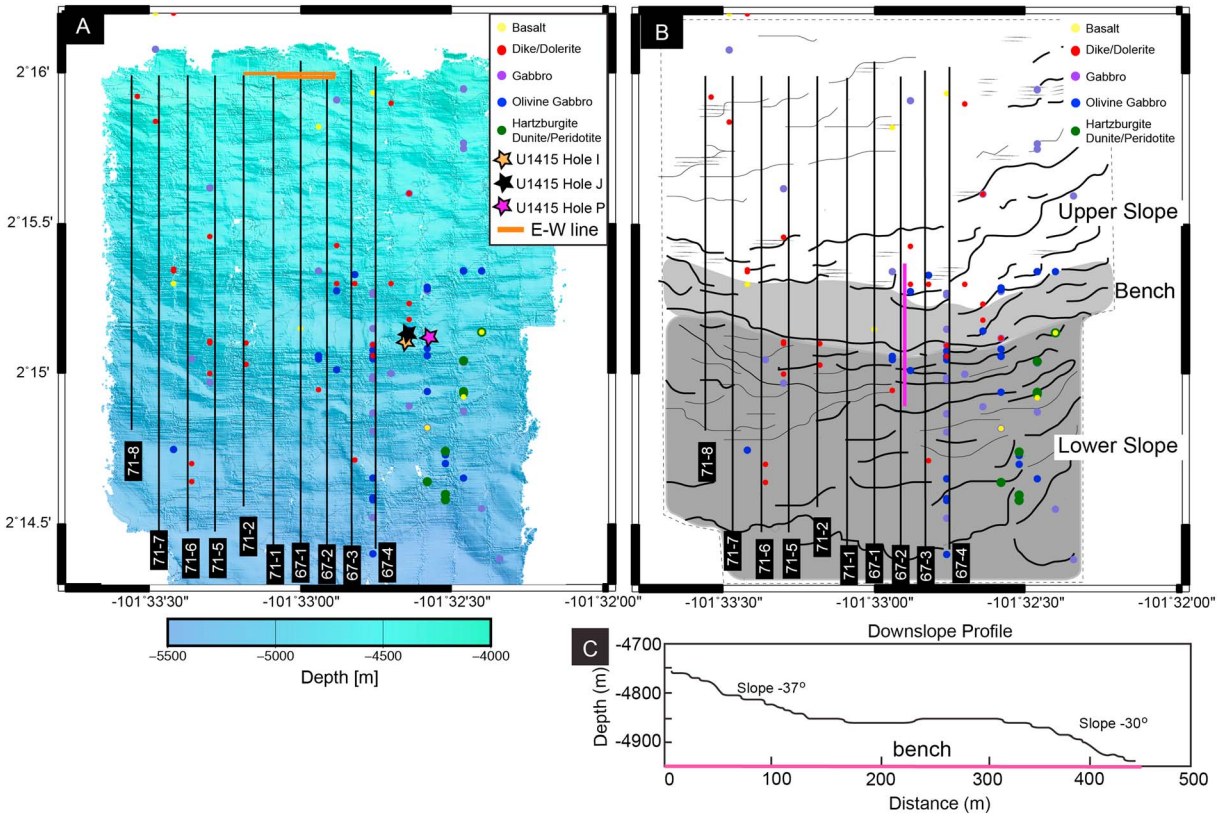

Figure 3. (a) Detailed map of the south facing slope of Hess Deep showing the near-bottom magnetic track lines. The base map is a compilation of shipboard bathymetry and ROV microbathymetry data from *Ferrini et al.* [2013]. The line numbering is the convention used during the JC21 expedition. The orange line is the cross-track line for checking the data quality in between dives 67 and 71 (Figure S2 in the supporting information). Rock samples collected during JC21 and IODP Expedition 345 Site U1415 Holes I, J, and P, where gabbro samples were cored [*Gillis et al.*, 2014], are also indicated and (b) simplified ROV microbathymetry overlain by magnetic track lines and sample locations. Magenta line shows the location of the profile in C. (c) N-S cross section of the bench topographic feature in the middle of the slope (modified from *Ferrini et al.* [2013]).

with considerable inclination scatter; and (b) data from IODP Hole U1415P, in contrast, show that the top 60 mbsf has a mean inclination of $-55° \pm 9.2°$ overlying a zone from 60 to 100 mbsf with a mean inclination of $-30.8° \pm 13.5°$[*Gillis et al.*, 2014].

2.2. Hess Deep Magnetism

Crustal magnetic investigations provide important insight into the formation of the Hess Deep region. Magnetic field results from *Alvin* dives on the north wall of Hess Deep reveal a weakly magnetized sheeted dike complex and dike-gabbro transition zone [*Tivey and Christeson*, 1999; *Varga et al.*, 2004]. *Alvin* dives 3379 and 3380 along the north wall show reverse polarity (negatively magnetized) crust at these locations consistent with their inferred spreading history [*Tivey and Christeson*, 1999] (Figures 1b and 1d).

Within Hess Deep on the intrarift ridge, paleomagnetic and rock magnetic results from 124 discrete gabbro samples recovered at ODP Hole 894G (Figures 1b and 2) show a mean natural remanent magnetization (NRM) of 2.2 A/m [*Kikawa et al.*, 1996; *Pariso et al.*, 1996]. The stable direction of the characteristic remanent magnetization (ChRM) has a median inclination of +45° (averaged values from $+51.2° \pm 13.9°$ by *Kikawa et al.* [1996] and 38° by *Pariso et al.* [1996]). A total of 67 harzburgite and 170 dunite discrete samples from ODP Site 895 yielded mean NRM values of 1.6 and 3.1 A/m, respectively. Harzburgites and dunites recovered from ODP Site 895 were typically more than 70% serpentinized [*Arai and Matsukage*, 1996; *Früh-Green et al.*, 1996; *Mével and Stamoudi*, 1996]. The median Koenigsberger ratio of these samples was about 2.4, consistent with this level of serpentinization and indicating a strong remanent magnetization component. The average ChRM inclination for samples from Site 895 (Figures 1b and 2) is $+55.7° \pm 22.7°$ [*Kikawa et al.*, 1996].

Measured mean inclinations for the ODP and IODP rock samples are much steeper than expected at this equatorial location [*Kikawa et al.*, 1996]; the expected inclination of the Geocentric Axial Dipole (GAD) is +4.6° and the IGRF-11 present-day field [*Finlay et al.*, 2010] has an inclination of +17.6° and declination of +8°. Drill cores, in general, lack declination data so that the polarity of the contemporaneous geomagnetic field of the inclination values must be constrained by additional regional tectonic constraints. To produce the observed steep inclinations, there are two scenarios based on the polarity of the crust. In the first scenario, the intrarift ridge basement is assumed to have been magnetized with normal polarity and was subsequently tilted northward by 51° (i.e., based on the difference between the averaged inclinations at ODP Sites 894 and 895 and the GAD of +4.6°, *Kikawa et al.* [1996]; *Pariso et al.* [1996]). In the second scenario, the basement was magnetized during a reverse polarity period, and the inclination was steepened by a 55–60° rotation toward the south on a north dipping fault. The regional tectonic and structural features and core-log integration study by *MacLeod et al.* [1996] are more consistent with the first scenario where the holes are located in the positively magnetized crust and rotated on a south dipping fault. *MacLeod et al.* [1996] also suggest a vertical axis rotation of 30° counterclockwise (i.e., to a declination of ~330°) as a result of the EPR and Cocos-Nazca rift interaction based on their core reorientation study.

2.3. Cruise JC21 Overview

Data in this study were obtained during RRS *James Cook* Cruise JC21 (6 January–10 February 2008) as part of a site survey conducted to support IODP Expedition 345 [*Gillis et al.*, 2014]. The objective of the cruise was to investigate lower oceanic crust exposed in Hess Deep using high-resolution near-bottom geophysics and sampling using the British ROV *Isis*. One of the designated survey sites was the south facing slope that flanks the deepest part of the rift valley where IODP Expedition 345 drill Site U1415 was eventually located (Figure 3a). New swath bathymetric data collected by the vessel's shipboard EM120 multibeam sonar improved the regional morphological data over Hess Deep rift valley and vicinity [*Ferrini et al.*, 2013] (Figures 1 and 2).

We also collected near-bottom microbathymetry data on the south facing slope (Figure 2) using a Simrad SM2000 multibeam sonar mounted on ROV *Isis* on multiple dives [*Ferrini et al.*, 2013]. Near-bottom magnetic data were collected on two of these dives (Dives 67 and 71 in Figure 3a). ROV *Isis* carried out this geophysical survey at an altitude of 100 m above the seafloor with 200 m line spacing (Figure 3). Following this mapping, ROV *Isis* was employed to visually image and document the in situ basement exposures to determine the distribution of lithology types and to collect rock samples. ROV dive videos show the region to be dominated by talus interspersed with in situ rock exposures along the survey tracks.

The most prominent individual feature on the slope is visible in the microbathymetry data as a flat "bench-like" (terrace) feature at ~4800 m water depth (Figure 3b) [*Ferrini et al.*, 2013]. Other important features associated with this terrace include consecutive semicircular scars on the slope face (Figures 2 and 3) and a lobe-shaped toe, the latter appearing to be a common morphology in the lower slopes of the Hess Deep rift valley (Figure 2).

We obtained a total of 93 samples from our study area in the south facing slope (Figures 2 and 3). Petrological observations and geochemical studies of the recovered ROV samples document the lithological distribution of dike, gabbros and (oxide-)gabbros, olivine gabbros, and serpentinized peridotite. Partially serpentinized peridotites dominate in the SE corner of the study area (Figure 3), and transition to troctolites, primitive olivine gabbros and evolved oxide gabbros/gabbronorites, and eventually to diabase (basaltic dikes) with an EPR-like chemistry [*MacLeod et al.*, 2008; *Lissenberg et al.*, 2013] toward the NW corner of the study area.

The remanent magnetization of representative basaltic dike and gabbro samples were measured at the Paleomagnetism Laboratory, Plymouth University, UK. The average NRM of basaltic dike samples is 0.61 ± 0.24 A/m (5 samples) and for the gabbros is 1.17 ± 2.3 A/m (58 samples) (Table 1). It is important to be aware that these rock samples were recovered from in situ outcrops that have undergone seafloor weathering, which can modify primary magnetic phases thereby potentially reducing the original magnetization intensity [e.g., *Irving et al.*, 1970].

Finally, high-precision U-Pb dating of zircon minerals from gabbroic rocks collected by the JC21 cruise at the western end of the intrarift ridge show that these gabbros were formed between 1.27 and 1.42 Ma, i.e., during the Matuyama reversed polarity epoch [*Rioux et al.*, 2012].

Table 1. Natural Remanent Magnetization Measurements on Dives 69, 70, and 73 Samples

Specimen	NRM Intensity A/m	Lithology
69R4A	0.13	gabbro
69R4B	0.08	gabbro
69R6B	1.47	troctolite
69R10B	0.52	disseminated oxide gabbro
69R14B	0.73	olivine gabbro
69R16B	0.92	oxide gabbro
70R1A	0.99	olivine gabbro
70R1B	0.25	olivine gabbro
70R1C	0.36	olivine gabbro
70R2A	3.47	olivine gabbro
70R2B	3.49	olivine gabbro
70R2C	1.98	olivine gabbro
70R10A	1.06	gabbro
70R10B	0.73	gabbro
70R14B	1.41	olivine gabbro
70R15B	0.03	olivine gabbronorite
70R17B	1.94	disseminated oxide gabbro
70R18B	4.04	oxide diorite
70R20B	1.56	oxide diorite
73R2B	0.52	olivine gabbro
73R4A	0.32	olivine gabbro
73R4B	0.11	olivine gabbro
73R4C	0.22	olivine gabbro
73R5A	0.07	olivine gabbro
73R7A	0.39	Cocos-Nazca basalt
73R7B	0.72	Cocos-Nazca basalt
73R7C	0.66	Cocos-Nazca basalt
73R7D	0.63	Cocos-Nazca basalt
73R9B	7.18	orthopyroxene-bearing olivine oxide gabbro
73R13A	0.19	gabbro
73R13B	0.20	gabbro
73R13C	0.17	gabbro
73R14A	0.14	gabbro
73R14B	0.20	gabbro
73R14C	0.18	gabbro
73R15B	0.04	orthopyroxene-bearing gabbro
73R16A	1.00	troctolitic gabbro
73R18B	0.12	olivine gabbro
73R20B	0.03	olivine-bearing gabbro

3. Methods

3.1. External Field Variations

A correction for diurnal variation is critical to the analysis of magnetic data acquired near the equator because the daily variation in Earth's magnetic field can easily be ±50 nT due to changes in solar ionization ("electrojet") of the Earth's ionosphere [e.g., *Onwumechilli*, 1967]. We obtained records of Earth's magnetic field total intensity for the JC21 cruise time period from the Teoloyucan Magnetic Observatory (19.75°N, 99.2°W), the longitudinally closest magnetic observatory to our survey site (data are publicly available at Space Physics Interactive Data Resource, http://spidr.ngdc.noaa.gov/spidr). There was only one magnetic storm (2 February 2008) during this period, and the remainder of the period is relatively quiet. Both dives 67 and 71 and the sea surface magnetic survey were collected outside of the magnetic storm period. The diurnal variation was retarded by 3 h to account for the longitude difference between the magnetic observatory and the center location of our survey site. We used the averaged diurnal variation profile from this observatory data set, excluding the magnetic storm, to correct both the sea surface and near-bottom magnetic data.

3.2. Sea Surface Magnetic Data Collection and Processing

Sea surface magnetic data were collected during cruise JC21 using a Marine Magnetics SeaSPY magnetometer sensor towed 280 m behind the ship at ~5.1444 m/s. We merged the magnetic and navigation data by calculating the position of the magnetometer with respect to the ship's GPS-based position. The resampled sea surface data were corrected for the International Geomagnetic Reference Field (IGRF)-11 model [*Finlay et al.*, 2010] to obtain the total field magnetic anomaly. For reference, the average total magnetic field observed at this location during our survey period was 41,493 nT. We combined these new JC21 sea surface magnetic data with previously collected sea surface magnetic data over the Hess Deep rift valley area available from the National Centers for Environmental Information (cruise IDs: CCTW02MV, CERE03WT, DI110L1, ENCR01WT, PLDS01MV, PPTU02WT, and VAN01MV). We compiled eight previous sea surface magnetic surveys over the Hess Deep rift valley. The average cross-over error between each data set was calculated using the x2sys program package [*Wessel*, 1989, 2010]. Cross-over errors were reduced from 29.2 to 3.7 nT by using a linear spline interpolator to level each of the track lines [*Wessel*, 2010]. The final compiled magnetic data were then interpolated onto a 0.25′ spaced grid using the GMT software minimum-curvature algorithm with a tension parameter of 0.25 (Figure 1c). At this equatorial latitude with the low geomagnetic field inclination, magnetic anomalies have an almost 180° phase shift such that the negative magnetic anomaly over the Cocos-Nazca spreading

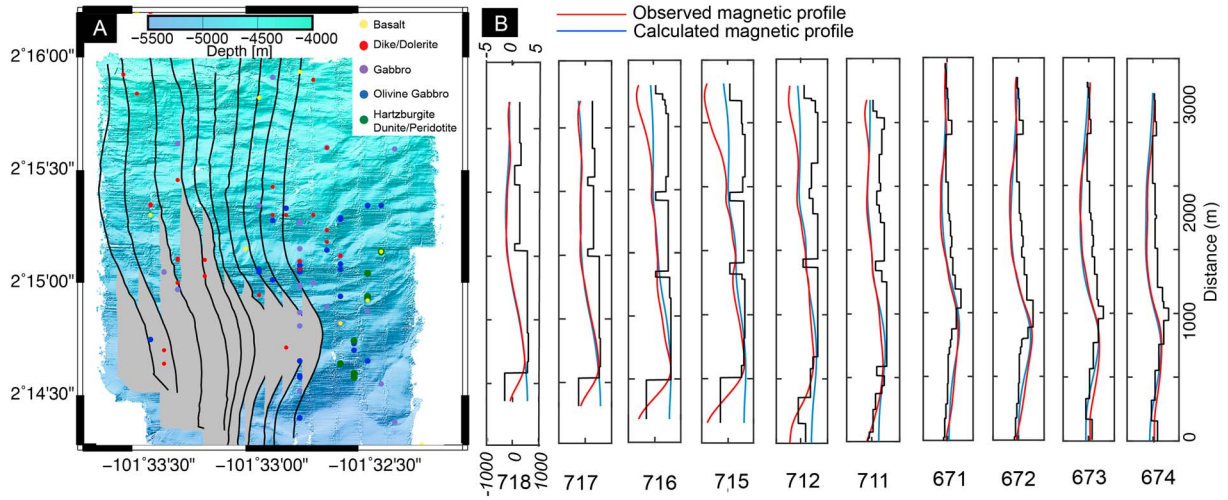

Figure 4. (a) Observed magnetic anomalies over the south facing slope of Hess Deep. (b) Track-by-track forward modeling results. The red and blue solid lines indicate modeled and observed anomalies, respectively. The black solid lines indicate the final intensity of magnetization for the block models (A/m). See the detailed calculation method in section 3.4.2.

indicates normal polarity Brunhes crust. Reduction-to-the-pole [*Spector and Grant*, 1970; *Blakely*, 1995] is inherently unstable at this latitude so we have chosen to simply refer to the observed anomaly map (Figure 1c) keeping in mind that we are dealing with a 180° phase shift.

3.3. Near-Bottom Magnetic Data Collection and Processing

Near-bottom three-component magnetic field data were collected by ROV *Isis* (dives 67 and 71) using a three axis Honeywell HMR2300 magnetometer mounted on the vehicle. The magnetometer has an intrinsic accuracy of ±4 nT and was mounted in a position on the ROV to minimize electrical interference and other sources of magnetic noise. The magnetic sensor was calibrated for both the permanent and induced field effects of the ROV. Considerable variation can be recognized between track lines in opposite heading directions particularly in low-latitude survey areas where the horizontal component is dominant in the ambient geomagnetic field. For this study, we built a calibration profile from the east-west turns within survey profiles to calculate the calibration coefficient matrix.

ROV magnetic field data were corrected for the vehicle's permanent and induced magnetization and motions (heading, pitch, and roll) based on the calibration routines established by *Isezaki* [1986], *Seama et al.* [1993], and *Korenaga* [1995]. ROV depth and altitude were obtained from a Paroscientific and Doppler altimeter, respectively, while the vehicle heading, pitch, and roll information were obtained from an Octans fiber optic gyrocompass. All the data, including magnetic field measurements, navigation, and vehicle attitude data were merged and processed based on time (i.e., all the sensor clocks were in sync with the vehicle clock). The calibration turns reduced the magnetic effect of the submersible on the sensor from 10,000 nT to less than 1,000 nT for both heading directions (uphill and downhill) (see also Figure S1 in the supporting information). There was no significant heading correction necessary.

After correction for the ROV vehicle-induced magnetization, we merged the vector magnetic data with the ROV navigation data. Navigation data utilized a ship-based ultrashort baseline system that was corrected based on the ROV microbathymetry and doppler velocity log positions [see *Ferrini et al.*, 2013].

To obtain vector magnetic anomaly components due to the magnetized lithosphere, we used the vehicle-corrected magnetic data merged with navigation and removed the present-day IGRF-11 model, i.e., inclination (17.6°), declination (008°), horizontal component (30,207 nT), and vertical component (4,273 nT) [*Finlay et al.*, 2010]. An IGRF value of 31,741 nT was subtracted from the total field data.

3.4. Magnetic Modeling

3.4.1. Cleaning and Resampling of Data

Ten near-bottom magnetic profiles from ROV *Isis* dives 67 and 71 were used in this study (Figure 4a) with the following survey characteristics: (1) north-south oriented track lines, (2) an east-west tie line to check

consistency between profiles (Figure 3a, also see Figure S2 in the supporting information), (3) a constant observation level above the slope surface (~101 m), and (4) lateral coverage from east to west with equally spaced track lines (~200 m), providing a consistent length scale for interpreting the results. There was no significant difference in anomaly baseline between upslope (northward) tracks and downslope (southward) tracks.

We "cleaned" both the vector and total anomaly data by removing portions of the track lines during periods when the ROV was being maneuvered at the end of lines or during sampling operations. Next, we resampled the 1 Hz vector components and total field onto a uniform along-track spacing of 3 m for subsequent Fourier transform processing.

3.4.2. Parameterization From Forward Modeling Results

Solutions derived from potential field modeling are nonunique, and so we use the principle of Occam's Razor to seek the simplest source structure in the total and vector-VMP modeling that fits the data. In the case of Hess Deep, we have constraints on the inclination value and polarity of magnetization from previous drilling results [*Kikawa et al.*, 1996]. Particularly important for our study is the premise, in order to explain the regional tectonic history, that the serpentinization of lower crust and upper mantle predates the rotation of the intrarift ridge [*MacLeod et al.*, 1996]. We conducted forward and inverse modeling using parameters suggested from the ODP Leg 147 drilled sites.

We first calculated a forward model of the observed magnetic field for each profile based on an analytic solution using first-order polygonal magnetic sources [*Talwani and Heirtzler*, 1964]. The remanent magnetic source is composed of 3×3 m square polygons with an effective in situ inclination of +51° and a declination of 330°, which are the average inclination value from the ODP Leg 147 results [*Kikawa et al.*, 1996; *Pariso et al.*, 1996] and the declination derived from core-log integration results [*MacLeod et al.*, 1996]. Note that these values are assumed to represent the original remanent magnetization from serpentinization that has subsequently been rotated tectonically. The ambient present-day inclination and declination values used are 17.6° and 008°, respectively [i.e., *Finlay et al.*, 2010]. We incorporated the 20° slope angle by rotating the calculation reference frame, yielding in situ effective inclination of +71° and present-day inclination of 37.6° in our model. The strike of the magnetic bodies is east-west (i.e., 90° from the north) and slope dips 20° toward the south. In our survey area, we do not know the exact location of the magnetite Curie isotherm (~580°C) at the Hess Deep Rift Valley system, which would define the depth limit of any lithospheric magnetization source layer. We note that the adjacent EPR crust located 100 km from the spreading axis (66 mm/yr half-spreading rate) yields a 600°C isotherm at approximately 10 km below the seafloor [e.g., *Braun et al.*, 2000]. However, for this study, we assumed a nominal constant source layer thickness of 1.0 km, which is consistent with the previously interpreted vertical extent of the gabbroic layer at Hess Deep [*Wiggins et al.*, 1996; *Ballu et al.*, 1999].

Starting with an initial model with a constant magnetization and fixed inclination values along the track lines, we carried out iterations to match the calculated total magnetic field to the observed total field by adjusting magnetization intensity values both in the positive and negative direction (i.e., implying either normal or reverse polarity).

Forward modeling results from all the ROV dive tracks indicate that the south facing slope is weakly positively magnetized with a few negatively magnetized blocks (Figure 4b). Magnetization values vary from −8 to +8 A/m along track, with median and mean values of 0.7 and 0.45 A/m, respectively. The overall distribution of magnetization intensities show that the upper slope is weakly magnetized compared with the lower slope. The magnetization distribution is also coherent from east to west between dive tracks 674 to 712 with a strong lateral correlation of the negatively magnetized segments at the location of anomaly peaks. The four western dive tracks 715 to 718 show an overall decrease in magnetization intensity from east to west (Figure 4b).

3.4.3. Total Field: Vertical Magnetic Profile (VMP) Inversion Analysis

We conducted magnetic inversion modeling of the corrected total magnetic field anomaly data using the vertical magnetic profile (VMP) approach established by *Tivey* [1996] (Figure 5a). With this method, given some basic assumptions about the polarity and inclination of the source region, we can calculate the total magnetic field response of in situ magnetic sources on a slope-oriented east-west. This method is particularly helpful when the magnetic profile is measured along a sloping surface as it avoids overfiltering the observed signal by having to upward continue to a level plane from the bottom of the slope to the upper part of the

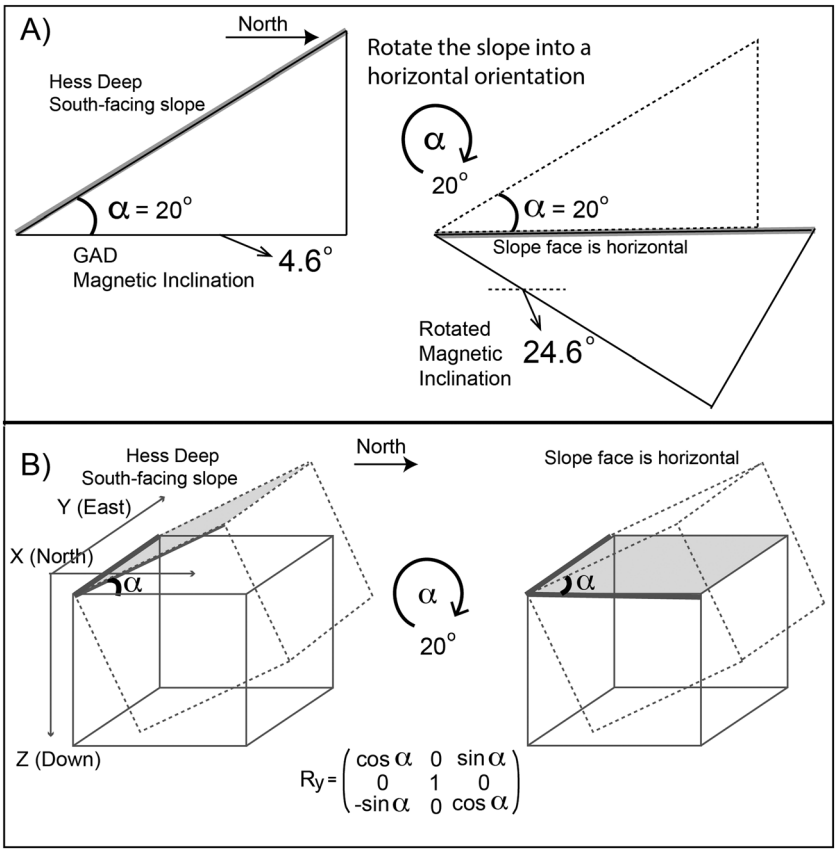

Figure 5. (a) Vertical Magnetic Profiling (VMP) rotation scheme. Suppose initial slope angle is α (in the case of the south facing slope of the Hess Deep, this is 20°), the rotation to make the VMP calculation will add α to the in situ inclination value [*Tivey*, 1996]. (b) The rotation scheme in the Vector Vertical Magnetic Profiling (VVMP) along a west-east extending (*y* axis), south facing slope in the northern hemisphere. Suppose initial slope angle is α (in the case of the Hess Deep south facing slope, this is 20°), the rotation to make the VVMP calculation will modify the *x* (north) and *z* (down) vector components.

slope. Essentially, the VMP method is a geometrical transformation that rotates the slope about its average slope angle into a level, slightly undulating surface, so that the original coordinates of the profile along the slope are also rotated and upward continuation to a new horizontal plane within this rotated frame of reference. In this approach only minimal filtering is incurred following *Guspi*'s [1987] upward continuation. This new level plane within the new "slope" reference frame is used to calculate the inversion for magnetization using the *Parker and Huestis* [1974] approach.

We used the following parameters for the VMP inverse modeling: a long- and short-wavelength cutoff of 3.25 km (equal to 12 h s) and 0.2 km, respectively; an in situ magnetization inclination of +51° with an average slope angle of ~20° and a declination of 330° [*MacLeod et al.*, 1996]; and a present-day effective ambient magnetic field inclination of 17.6° and a declination of 8°. In our calculation, we incorporated the 20° slope angle by rotating the calculation reference frame, yielding in situ effective inclination of +71° and present-day inclination of 37.6° in our model.

3.4.4. Vector Vertical Magnetic Profile (VVMP) and Directional Analyses

In addition to total field, we conducted a vector field analysis of the near-bottom three-component magnetic data to characterize in situ magnetic sources with additional information on the location and trends of possible magnetic and structural boundaries [e.g., *Seama et al.*, 1993; *Korenaga*, 1995; *Lee and Kim*, 2004].

Starting with the diurnal-, vehicle-, and IGRF-11 model-corrected three-component magnetic field data, we used a modified version of the VMP method [*Tivey*, 1996] that accommodates the three magnetic components of *x*: north, *y*: east, and *z*: vertical (i.e., our Vector-VMP or VVMP method) (Figure 5b). To rotate the data into the horizontal plane in the same manner as the VMP method, the overall geometry of the west-east striking south facing slope becomes useful. We take the west-east direction (*y*) as a fixed axis and then make

a new coordinate system rotating the *x* and *z* axes around the *y* axis using the average slope angle (Figure 5b). The rotated three-component data were then resampled and upward continued to a level observation plane within this rotated reference frame.

We then use the rotated vector field data to obtain the deviation from two dimensionality of the magnetic sources [*Isezaki*, 1986; *Korenaga*, 1995] as well as a structural index by calculating the intensity of spatial differential vectors (ISDV) [*Seama et al.*, 1993].

The deviation from two dimensionality of the magnetic sources in this study is primarily indicative of the linearity of the magnetic source. Theoretically, this linearity of the source is evaluated by comparing the observed (H_{obs}) and theoretical (H_{2d}) horizontal components of the anomaly data [*Isezaki*, 1986]. Previous studies evaluated the deviation from a two-dimensional source (i.e., the amount of "three dimensionality") based on the residual power of the signal-to-noise ratio [*Korenaga*, 1995; *Lee and Kim*, 2004; *Sato et al.*, 2009]. We instead used the difference between H_{obs} and H_{2d} directly to show the distribution of the deviations because (1) the ROV data have an optimal signal-to-noise ratio and (2) the power density spectrum of our profile contains meaningful spectra over the entire wave number domain (our profiles are 3 km long with a wave number of 0.33 km^{-1}), and therefore Wiener filtering used by *Korenaga* [1995] is not required for our case.

To identify magnetic boundaries using three-component magnetic vector anomalies, *Seama et al.* [1993] proposed using the ISDV approach. ISDV as defined by *Isezaki* [1986] and *Seama et al.* [1993] is the vector sum (intensity) of changes in each of the three crustal magnetic field components (differential vectors) along a ship track coordinate assuming a purely 2-D magnetic source, i.e., if the crustal magnetic field direction is parallel to a boundary direction within a magnetic source, the ISDV is zero. The advantage of using the ISDV is that it reaches a maximum at a magnetic boundary (i.e., structural, lithological, or polarity), irrespective of the magnetization direction. We applied this technique to our vector magnetic anomalies to detect the location and trends of magnetic boundaries. The ISDV values are calculated at each observation point in the upward continued data. *Seama et al.* [1993] suggest that the resolution (the width of the detectable boundary) of the ISDV method is 1.5 times the water depth. For our near-bottom data, the relevant distance would be the water depth to the sensor, which given the nominal ROV altitude of 100 m, means that the ISDV data effectively includes all wavelengths down to a length scale of ~150 m.

4. Results

4.1. Sea Surface Magnetic Anomalies

Our new compilation of JC21 sea surface magnetic anomalies leveled with previously collected shipborne magnetic anomaly profiles and the EMAG2 grid [*Maus et al.*, 2009] document that (1) two Alvin dive traverses (dives 3379 and 3380) are within reversely magnetized crust consistent with the vertical profiling results by *Tivey and Christeson* [1999]; (2) Sites 894 and 895 are within the same reversely magnetized crust (Matuyama reverse polarity), but can also be projected into a normal polarity portion of the EPR crust, if we extrapolate Lonsdale's (1977) magnetic lineations on the EMAG2 map; (3) JC21 dives 67 and 71 are located directly south of this possible normal polarity portion of the EPR crust (Figure 1c); and (4) ODP Site 894 paleomagnetic results suggest that the crust has normal polarity, whereas the zircon U-Pb date from the ROV sample in the vicinity of ODP Site 894 suggests an absolute age of 1.27 Ma, within the reverse polarity Matuyama chron (Figure 1c).

4.2. Magnetization Distribution: VMP Inversion Results

The VMP inversion results along each of the 1-D profiles (dives 67: 1–4 and 71: 1–8) provide the simplest case of a 2-D magnetization distribution model for a constant thickness source layer. We observe several features in the VMP inversion results that are worthy of note. For simplicity, we divide the slope into an upper and lower parts based on the magnetization contrasts and underlying morphology (Figures 6a and 6b).

The major feature revealed by the VMP inversion is the overall coherency in regional magnetization character across the study area (Figures 6a and 6b). We can correlate peaks and troughs of magnetization between track lines. A strong magnetization contrast is found between the upper and lower parts of the slope. The location of this contrast is marked by a broad magnetization low and coincides with the bench between the upper and lower parts of the slope [*Ferrini et al.*, 2013] (Figures 6a and 6b). On the upper slope, magnetization character is subdued. On the lower slope, magnetization character is dominated by high-amplitude,

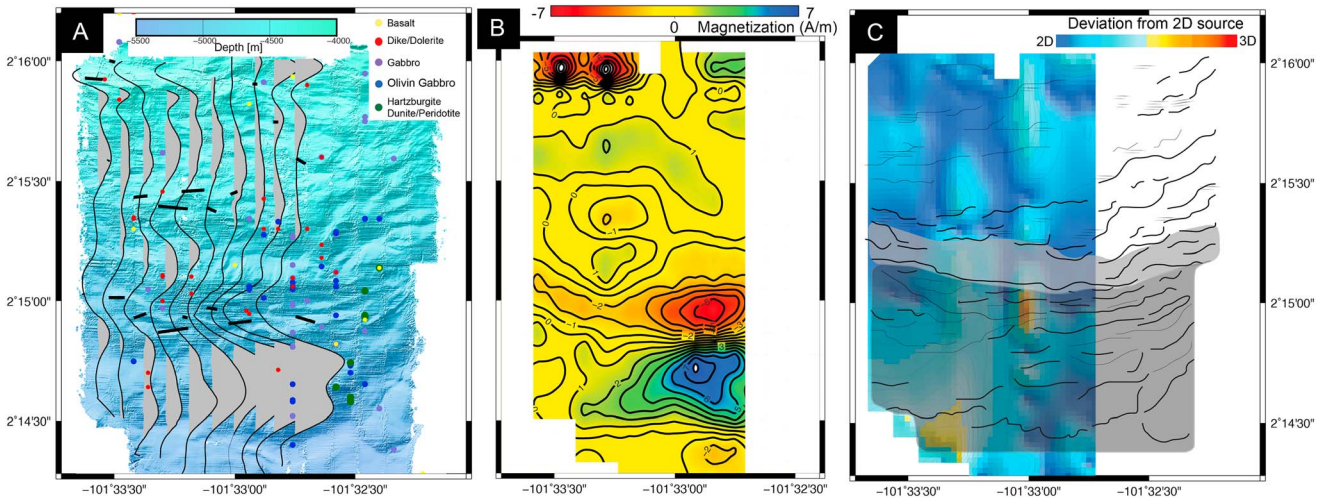

Figure 6. (a) Inversion results plotted over the microbathymetry data. The solid lines show the along-track inversion profiles (magnetization distribution along the tracks). The solid black bars indicate the locations of ISDV peaks with length proportional to their intensity (see section 3.4.4). (b) Gridded inversion results shown in Figure 6a. (c) Line drawing of the microbathymetry data (from Figure 3b) overlying a colored grid that shows the deviation in magnetization from a two-dimensional source, cf. the presence of three dimensional sources.

long-wavelength (500–1000 m) features with a gradual reduction in amplitude from east to west across the slope (Figures 6a and 6b).

4.3. VVMP Directional Analysis Results

Vector field magnetic anomaly analyses show a magnetic source character that is not captured either by the forward or inverse modeling approaches. The peaks in the intensity of the spatial differential vectors (ISDV) can result from topographic effects, geomagnetic field reversals, and magnetization contrasts [*Seama et al.*, 1993]. The distribution of calculated magnetic strikes based on the ISDV peaks are representative of different areas with internally consistent magnetic boundary orientations (Figure 6a). For the south facing slope of Hess Deep, these ISDV peaks potentially correspond to different combinations of strong deformation, rotation, faulting, and alteration of the underlying magnetized rocks. Throughout the slope, we observe two concentrations of ISDV peaks with similar orientations to the underlying morphology (Figure 6a). One is located in the middle part of the slope, which coincides with the termination of the upper slope at the bench and corresponds to the troughs in magnetization values on lines 711, 712, 715, and 716. The other is located at the edge of the lobe-shaped morphology in the lower slope that coincides with the broader trough in the magnetization from lines 674 to 716 (Figure 6a).

The three dimensionality of the source is characterized by the magnitude of the deviations from a two-dimensional source [e.g., *Talwani and Heirtzler*, 1964] and can be used to infer how the juxtaposition of magnetic boundaries within the underlying magnetic bodies deviate from a strike perpendicular to the survey track. On the south facing slope, there are two areas in the magnetic source region where significant deviations from a two-dimensional source are observed. The strongest deviation is located at the southwestern corner of the lower part of the slope where the magnetization values are the weakest. In the eastern middle part of the slope at the bench there is a smaller area of distinctive three dimensionality (Figure 6c).

5. Discussion

5.1. The Origin of the Coherent Magnetic Source at the Hess Deep

All the results from magnetic inversion and 3-D index analyses indicate that there is internally coherent magnetic source that produces (1) a high contrast between upper and lower slope magnetization amplitudes, the location of which is marked by the morphological bench situated at the middle of the slope (Figure 6); and (2) a systematic westward weakening of anomaly amplitude in the lower slope. The origin of this coherent magnetic source is likely to be a combination of in situ magnetization, structure, and lithology (i.e., rock and associated alteration types).

At present, there are no fully oriented samples widely distributed across the south facing slope to constrain polarity distributions. Even two closely located drilled holes on the bench (IODP Holes U1415J and U1415P, Figure 3a) exhibit formations with significantly different inclination values and polarity distributions both downhole and in between the two holes, suggesting the relatively shallow coring has only sampled the surficial disturbed zone of mass wasting [*Gillis et al.*, 2014]. Even if fully oriented samples become available in deeper holes, however, their interpretation would likely be challenging because of complex, temporally and spatially variable, late-stage serpentinization of the mantle rocks [*Kikawa et al.*, 1996; *MacLeod et al.*, 1996]. Hence, our discussion will focus on deciphering the origin of changes in magnetic intensity on the south facing slope of the Hess Deep by documenting the geophysical footprint of the crustal architecture and internally preserved lithological evolution.

Although previous studies [e.g., *Francheteau et al.*, 1990; *MacLeod et al.*, 1996] tacitly assumed that the south facing slope comprised a 2-D section through a lithological layer cake of fast spreading oceanic lithosphere —upper mantle, lower, and the upper crust sections—we observe little systematic, stratigraphic, juxtapositions of such layer cake lithology based on the ROV sample distribution, except for two, broad assemblages of lower crustal/ultramafic rocks in the eastern lower part of the slope and upper crustal rocks in the upper part of the slope. The lithological contribution to the magnetic signatures can still be considered, but other magnetic sources are required to fully explain the observed magnetic signatures.

The internally coherent magnetic source found in the south facing slope suggests that the locally observed slope consists of mostly cohesive sliding units as a consequence of mass wasting. Seafloor slope observations in the Atlantic [e.g., *Mitchell et al.*, 2000; *Cannat et al.*, 2013] document the distinctive character of mass wasting (block sliding) of serpentinized seafloor—it behaves as cohesive slipped blocks where scars on the failing tectonic scarp can be semicircular, while the slipped block has lobe-shaped steps and a toe [*Cannat et al.*, 2013]. These morphological features are observed in the microbathymetry as a 100 m wide bench [*Ferrini et al.*, 2013] and as consecutive semicircular steps of cohesive slipped blocks with a thick, lobe-shaped toe (Figure 3). The hydrous minerals that compose the major lithology of serpentinized rocks would lead to slipped blocks having viscoplastic behavior so that fissures can develop with little fragmentation from internal deformation of the blocks [*Cannat et al.*, 2013], thereby preserving internal structure and lithology, as has been proposed for this region [*Ferrini et al.*, 2013]. The line-to-line coherency of magnetization distribution, particularly the coincidence between changes in magnetization character and ISDV peaks (Figures 6a and 6b) and the location of the midslope bench suggest that the source of the anomalies is not surficial.

The overall distinctive magnetic signatures are indicative of well-preserved internal structure to our surveyed area. The thickness and juxtaposition of the slipped block(s) and randomly overlying debris remain unknown, although paleomagnetic results from IODP Holes U1415-I, J, and P located on the bench (Figure 3a) indicate that at least the upper 35–60 m of the bench consists of rotated, displaced blocks by mass wasting [*Gillis et al.*, 2014]. However, even with a simple phase-shift test, where we assign additional 45° and 90° rotations to the inversion results, we still preserve the overall juxtaposition of highs and lows within the magnetization distribution (Figure S3 in the supporting information), indicating that the coherent magnetized source is likely due to a single slipped magnetized block extending to depth (at least to the modeled 1 km thickness) with polarity boundaries normal to the slope face rather than overlapping slipped blocks (thin slivers) with opposite polarities. Hence, our magnetic imaging likely reflects the internal magnetic source architecture of the footwall of the south facing slope.

The high-magnetization contrast at the bench of the slope is likely explained by a structural boundary that is related to the semicircular tectonic sole of the slipped block (Figures 6 and 7). Within the lower part of the slope below the sole, the westward weakening of the magnetization amplitude is attributed to a combination of changes in thickness, the randomness of rock emplacement by mass wasting processes, and variations in lithology (Figure 7).

In our study area, serpentinized peridotite samples are confined only to the easternmost side of the slope with olivine and oxide gabbros and basaltic dikes to the west, possibly explaining the westward weakening in magnetization amplitudes, because among these rock types (i) magnetization values of serpentinized peridotite can be much higher than that of basaltic dikes and gabbros depending on the degree of serpentinization [*Saad*, 1969; *Kikawa et al.*, 1996; *Dyment*, 1998; *Oufi et al.*, 2002; *Malvoisin et al.*, 2012a, 2012b] and (ii)

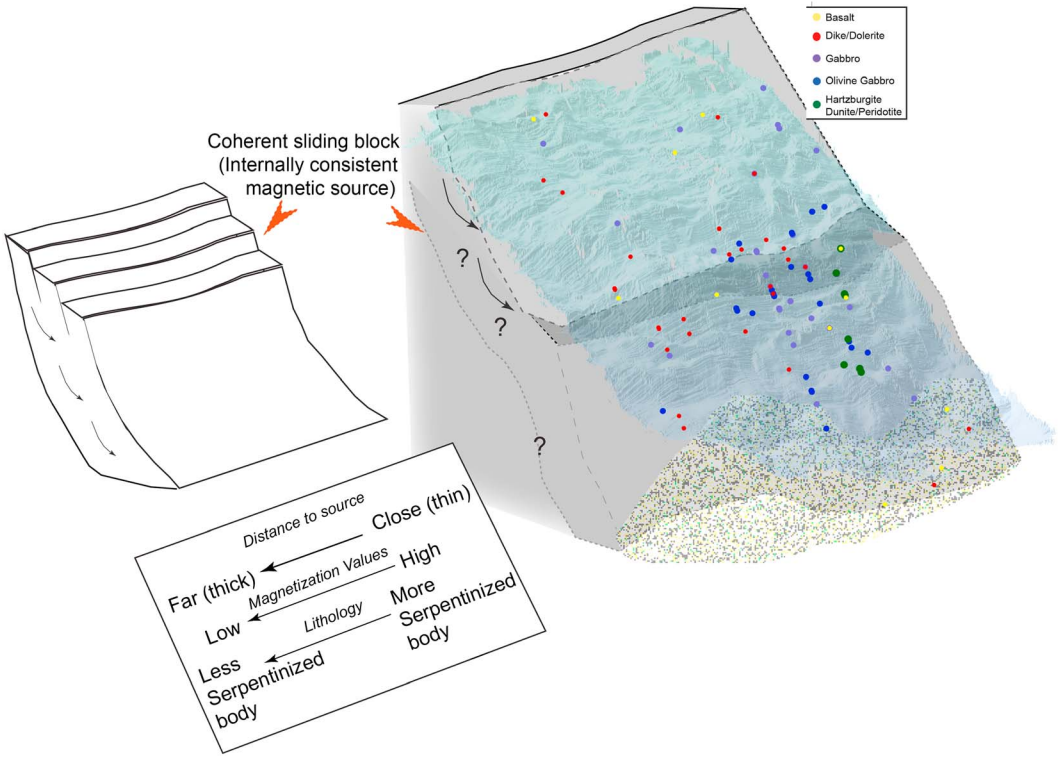

Figure 7. A schematic summary of magnetic sources of the Hess Deep south facing slope, with microbathymetry with color coded sample locations overlying the inferred slipped surface and the middle slope bench of *Ferrini et al.* [2013].

magnetization values of gabbroic rocks are typically less than those of serpentinized peridotite samples and typically vary depending on the mineralogy and cooling history [*Kent et al.*, 1978; *Luyendyk and Day*, 1982; *Gee and Meurer*, 2002; *Hosford et al.*, 2003; *Varga et al.*, 2004; *Garcés and Gee*, 2007; *Maffione et al.*, 2014]. The magnetization of the dike section as a whole has been found to be relatively weak [e.g., in ODP Hole 504B; *Pariso and Johnson*, 1991] especially compared to other crustal sections and so our results appear broadly consistent with this distribution. In addition, microbathymetry of the south facing slope indicates that the lobe-shaped toe of the slide appears to thicken westward, where the strongest deviation from the two dimensionality is also observed, suggesting that the western side of the lower part of the slope has a different mass wasting emplacement style (Figures 6 and 7). Although true thickness and randomness of the debris in the lobe-shaped toe are unknown, increasing the distance to any coherent source will also reduce magnetization amplitudes. Thus, the westward weakening in the magnetization intensity appears to capture the lithological variation from serpentinized peridotite in the southeast part of the slope study area to more weakly magnetized rocks, such as olivine gabbros, gabbros, and basaltic dikes, the magnetic signal of which are further attenuated by westward thickening of the emplaced rocks as a result of the sliding process (Figure 7).

5.2. Chronology of Intrarift Ridge Crustal Samples and Implications for the Evolution of Magnetizations in Hess Deep

There is an apparent discrepancy between inferred magnetic polarity between two closely (~500 m) located sites on the Intrarift Ridge, between the ODP drill sites and the sample location for zircon dating (Figure 1b). The magnetic polarity suggested based on gabbro samples from ODP drill sites shows normal polarity, whereas zircon dates imply gabbro crystallization during reverse polarity. Although this discrepancy initially appears puzzling, unraveling its chronology helps us decipher the evolution of the Hess Deep rifting system.

The U-Pb zircon age of the crust is derived independently from magnetic acquisition processes. The closure temperature for the U-Pb system in zircon (~850°C) is close to the crystallization temperature of the gabbro and significantly higher than the Curie temperature of magnetite (580°C) and a typical blocking temperature

range of 580–550°C. Hence, the zircon ages of ~1.27 Ma mark the time that the Hess Deep section crystallized [*Rioux et al.*, 2012], which is in the Matuyama reverse polarity chron (0.781–2.581 Ma) [*Gradstein et al.*, 2012]. The crust would become magnetized slightly later, either in the Cobb Mountain (1.173–1.185 Ma) or Jaramillo (0.988–1.072 Ma) normal polarity subchrons of the current geomagnetic polarity time scale [*Gradstein et al.*, 2012] as the crust cooled through its magnetic blocking temperature range.

Magnetization acquisition processes within lower crust and upper mantle formations could be thermal in origin but may also be attributed to late stage chemical alteration, and particularly, chemical remanent magnetization associated with intense serpentinization [e.g., *Kikawa et al.*, 1996; *Pariso et al.*, 1996; *Oufi et al.*, 2002; *Malvoisin et al.*, 2012a, 2012b; *Maffione et al.*, 2014]. Such late stage chemical alteration has been invoked for the magnetization of formations in both ODP Holes 894 and 895 based on core-log integration and on local tectonic reconstruction [*MacLeod et al.*, 1996].

Given the timing of the formation of the crust inferred by the zircon data from the gabbro samples, the normal polarity magnetization observed in the south facing slope could have been acquired in a later normal polarity period than the original remanent magnetization, as a result of chemical magnetization arising from serpentinization. This could have occurred during either during the Cobb Mountain, Jaramillo, or Brunhes (i.e., today's magnetic field) normal polarity period.

Combining the zircon absolute age data and the state of highly serpentinized samples from both ODP Holes and our ROV rock sampling, we propose that the most feasible sequence of events affecting the samples from each site is as follows: (i) in situ gabbro at EPR is formed during the Matuyama reverse polarity chron represented by the zircon age [*Rioux et al.*, 2012], followed by the acquisition of an original thermoremanence by the gabbros of the intrarift ridge; (ii) alteration and serpentinization of these EPR gabbros and upper mantle peridotite, respectively, resulted in a chemical remanent magnetization being acquired during one of the later normal polarity periods; and (iii) rifting created the intrarift ridge and exposed these gabbros and serpentinized peridotites on the south facing slope of Hess Deep.

6. Conclusions

We summarize our conclusions from this study as follows:

1. Line-to-line coherency of magnetization distribution may be an indication of a well-preserved internal structure in cohesive slipped blocks that comprise the south facing slope of the Hess Deep. The distinctive contrast in magnetization amplitude between the upper and lower slopes is likely to be attributed to the middle slope bench, one of the semicircular, steplike scars resulting from block slippage.
2. The westward weakening of magnetization intensity in the lower part of the slope appears to capture the lithological variation from serpentinized peridotite in the southeast part of the slope study area to more weakly magnetized formations, such as olivine gabbros, gabbros and (oxide-) gabbros, and basaltic dikes. The amplitude of the magnetic signal from these rocks is likely to be further attenuated by westward thickening of the rocks emplaced by the sliding process (i.e., the thickness of the toe lobes overlying the source rock formation). These survey lines therefore document the first magnetic profiles that capture the gabbro-ultramafic and possibly dike-gabbro boundaries in fast-spreading lower crust.
3. In combination with previously reported analyses, our data suggest the following sequence of events in the evolution of magnetization in Hess Deep: (i) acquisition of an original thermoremanent magnetization by in situ gabbros at the EPR during the Matuyama reverse polarity chron; (ii) alteration and serpentinization of these EPR gabbros and peridotite, resulting in acquisition of chemical remanent magnetizations during one of the Cobb, Jaramillo, and Brunhes normal polarity periods; and then, (iii) rifting of the intrarift ridge to expose these rocks on the south facing slope at the Hess Deep.

Acknowledgments

We thank the JC21 shipboard scientific party, the captain and crew on the RRS *James Cook*, and ROV *Isis* engineers and technicians from the UK National Oceanography Centre. This study was supported by NERC grant NERC509023/1 (MacLeod), IODP-USSSP grant (Shillington and Ferrini), and Woods Hole Oceanographic Institution Postdoctoral Scholarship (Tominaga). Enquiries regarding the JC21 data used in this study should be directed to the project's principal scientist, MacLeod at Cardiff University (macleod@cardiff.ac.uk). We thank the Associate Editor André Revil, F. Caratori-Tontini, and an anonymous reviewer for their constructive comments that improved this manuscript.

References

Allerton, S., and M. A. Tivey (2001), Magnetic polarity structure of lower oceanic crust, *Geophys. Res. Lett.*, *28*, 423–426, doi:10.1029/2000GL008493.

Anonymous (1972), GSA Penrose field conference on ophiolites, *Geotimes*, *17*, 24–25.

Arai, S., and K. Matsukage (1996), Petrology of gabbro-troctolite-peridotite complex from Hess Deep, equatorial Pacific: Implications for mantle-melt interaction within the oceanic lithosphere, in *Proc. ODP, Sci. Results*, vol. 147, edited by C. Mével et al., pp. 135–155, Ocean Drilling Program, College Station, Tex., doi:10.2973/odp.proc.sr.147.008.1996

Arkani-Hamed, J. (1988), Remanent magnetization of the oceanic upper mantle, *Geophys. Res. Lett.*, *15*, 48–51, doi:10.1029/GL015i001p00048.

Baines, A. G., M. J. Cheadle, B. E. John, and J. J. Schwartz (2008), The rate of oceanic detachment faulting at Atlantis Bank, SW Indian Ridge, *Earth Planet. Sci. Lett.*, *273*, 105–114.
Ballu, V., J. A. Hildebrand, and E. L. Canuteson (1999), The density structure associated with ocean crustal rifting at the Hess Deep: A seafloor and sea surface gravity study, *Earth Planet. Earth Lett.*, *171*, 12–34.
Blakely, R. J. (1995), *Potential Theory in Gravity and Magnetic Applications*, 441 pp., Cambridge University Press, Cambridge, U. K.
Braun, M. G., G. Hirth, and E. M. Parmentier (2000), The effects of deep damp melting on mantle flow and melt generation beneath midocean ridges, *Earth Planet. Sci. Lett.*, *176*, 339–356.
Cannat, M., A. Mangeney, H. Ondreas, Y. Fouquet, and A. Normand (2013), High-resolution bathymetry reveals contrasting landslide activity shaping the walls of the mid-Atlantic Ridge axial valley, *Geochem. Geophys. Geosyst.*, *14*, 996–1011, doi:10.1002/ggge.20056.
DeMets, C., R. G. Gordon, and D. F. Argus (2010), Geologically current plate motions, *Geophys. J. Int.*, *181*, 1–80.
Dick, H. J. B., et al. (2000), A long in situ section of the lower oceanic crust: results of ODP Leg 176 drilling at the Southwest Indian Ridge, *Earth Planet. Sci. Lett.*, *179*, 31–51.
Dick, H. J. B., M. A. Tivey, and B. E. Tucholke (2008), Plutonic foundation of a slow spread ridge segment: The oceanic core complex at Kane Megamullion, 23°30′N, 45°20′W, *Geochem. Geophys. Geosyst.*, *9*, Q05014, doi:10.1029/2007GC001645.
Dyment, J. (1998), Contribution of lithospheric remanent magnetization to satellite magnetic anomalies over the world's oceans, *J. Geophys. Res.*, *103*, 15,423–15,441, doi:10.1029/97JB03574.
Escartin, J., D. K. Smith, J. Cann, H. Schouten, C. H. Langmuir, and S. Escrig (2008), Central role of detachment faults in accretion of slow spreading oceanic lithosphere, *Nature*, *455*, 790–794.
Ferrini, V. L., D. J. Shillington, K. Gillis, C. J. MacLeod, D. A. H. Teagle, A. Morris, P. W. Cazenave, S. Hurst, M. Tominaga, and the JC21 Scientific Party (2013), Evidence of mass failure in the Hess Deep Rift from multiresolutional bathymetry data, *Mar. Geol.*, *339*, 13–21.
Finlay, C. C., et al. (2010), International geomagnetic reference field: The eleventh generation, International Association of Geomagnetism and Aeronomy, Working Group V-MOD, *Geophys. J. Int.*, *183*, 1216–1230.
Fox, P. J., and N. D. Opdyke (1973), Geology of the oceanic crust: Magnetic properties of oceanic rocks, *J. Geophys. Res.*, *78*, 5139–5154, doi:10.1029/JB078i023p05139.
Francheteau, J., R. Armijo, J. L. Cheminee, R. Hekinian, P. Lonsdale, and N. Blum (1990), 1 Ma East Pacific Rise oceanic crust and uppermost mantle exposed by rifting in Hess Deep (equatorial Pacific Ocean), *Earth Planet. Sci. Lett.*, *101*, 281–295.
Früh-Green, G. L., A. Plas, and C. Lécuyer (1996), Petrologic and stable isotope constraints on hydrothermal alteration and serpentinization of the EPR shallow mantle at Hess Deep (Site 895), in *Proc. ODP, Sci. Results*, vol. 147, edited by C. Mével et al., pp. 255–291, Ocean Drilling Program, College Station, Tex., doi:10.2973/odp.proc.sr.147.016.1996
Fujiwara, T., J. Lin, P. Matsumoto, B. Tucholke, and J. Casey (2003), Crustal evolution of the mid-Atlantic Ridge near the Fifteen-Twenty Fracture Zone in the last 5 Ma, *Geochem. Geophys. Geosyst.*, *4*(3), 1024, doi:10.1029/2002GC000364
Garcés, M., and J. S. Gee (2007), Paleomagnetic evidence of large footwall rotations associated with low-angle faults at the mid-Atlantic Ridge, *Geology*, *35*, 279–282.
Gee, J. S., and D. V. Kent (2007), Source of oceanic magnetic anomalies and the geomagnetic polarity time scale, in *Treatise on Geophysics, v. 5, Geomagnetism*, edited by M. Kono, pp. 455–507, Elsevier, Amsterdam.
Gee, J., and W. P. Meurer (2002), Slow cooling of middle and lower oceanic crust inferred from multicomponent magnetizations of gabbroic rocks from the mid-Atlantic Ridge south of the Kane fracture zone (MARK) area, *J. Geophys. Res.*, *107*(B7), 2137, doi:10.1029/2000JB000062.
Gillis, K. M., J. E. Snow, A. Klaus, and the Expedition 345 Scientists (2014), *Proc. IODP*, vol. 345, Integrated Ocean Drilling Program, College Station, Tex., doi:10.2204/iodp.proc.345.2014.
Gillis, K., et al. (1993), *Proc. ODP, Init. Repts*., vol. 147, Ocean Drilling Program, College Station, Tex., doi:10.2973/odp.proc.ir.147.1993
Gradstein, F. M., J. G. Ogg, M. D. Schmitz, and G. M. Ogg (2012), *The Geologic Time Scale*, 1144 pp., Elsevier, Boston.
Guspi, F. (1987), Frequency domain reduction of potential field measurements to a horizontal plane, *Geoexploration*, *24*, 87–98.
Harrison, C. (1987), Marine magnetic anomalies: The origin of the stripes, *Annu. Rev. Earth Planet. Sci.*, *15*, 505–543.
Hey, R. (1977), Tectonic evolution of the Cocos-Nazca spreading center, *Geol. Soc. Am. Bull.*, *88*, 1404–1420.
Honsho, C., T. Ura, and K. Tamaki (2012), The inversion of deep-sea magnetic anomalies using Akaike's Bayesian information criterion, *J. Geophys. Res.*, *117*, B01105, doi:10.1029/2011JB008611.
Hosford, A., M. Tivey, T. Matsumoto, H. Dick, H. Schouten, and H. Kinoshita (2003), Crustal magnetization and accretion at the southwest Indian Ridge near the Atlantis II fracture zone, 0–25 Ma, *J. Geophys. Res.*, *108*(B3), 2169, doi:10.1029/2001JB000604.
Hurst, S. D., J. A. Karson, and K. L. Verosub (1994), Paleomagnetism of tilted dikes in fast spread oceanic crust exposed in the Hess Deep Rift: Implications for spreading and rift propagation, *Tectonics*, 789–802, doi:10.1029/94TC00845.
Irving, E., W. A. Robertson, and F. Aumento (1970), The mid-Atlantic ridge near 45°N: VI. Remanent intensity, susceptibility, and iron content, *Can. J. Earth Sci.*, *7*, 226–238.
Isezaki, N. (1986), A new shipboard three component magnetometer, *Geophysics*, *51*, 1992–1998.
Johnson, G. L., P. R. Vogt, R. Hey, J. Campsie, and A. Lowrie (1976), Morphology and structure of the Galapagos Rise, *Mar. Geol.*, *21*, 81–120.
Johnson, H. P., and J. E. Pariso (1993), Do layer 3 rocks make a significant contribution to marine magnetic anomalies? In situ magnetization of Gabbros at Ocean Drilling Program Hole 735B, *J. Geophys. Res.*, *98*, 16,033–16,052, doi:10.1029/93JB01097.
Karson, J., S. Hurst, and P. Lonsdale (1992), Tectonic rotations of dikes in fast-spread oceanic crust exposed near Hess Deep, *Geology*, *20*, 685–688.
Kent, D. V., B. M. Honnorez, N. D. Opdyke, and P. J. Fox (1978), Magnetic properties of dredged oceanic gabbros and the source of marine magnetic anomalies, *Geophys. J. R. Astron. Soc.*, *55*, 513–537.
Kidd, R. G. W. (1977), The nature and shape of the sources of marine magnetic anomalies, *Earth Planet. Sci. Lett.*, *33*, 310–320.
Kikawa, E., and K. Ozawa (1992), Contributions of oceanic gabbros to sea floor spreading magnetic anomalies, *Science*, *258*, 796–799.
Kikawa, E., P. R. Kelso, J. E. Pariso, and C. Richter (1996), Paleomagnetism of gabbroic rocks and peridotites from Sites 894 and 895, leg 127, Hess Deep: Results of half-core and whole-core measurements, in *Proc. Ocean Dril. Prog. Sci. Res*, vol. 147, edited by C. Mével et al., pp. 383–391, Ocean Drilling Program, College Station, Tex.
Korenaga, J. (1995), Comprehensive analysis of marine magnetic vector anomalies, *J. Geophys. Res.*, *100*, 365–378, doi:10.1029/94JB02596.
Lee, S. M., and S. Kim (2004), Vector magnetic analysis within the southern Ayu Trough, equatorial western Pacific, *Geophys. J. Int.*, *156*, 213–221.
Lissenberg, C. J., C. J. MacLeod, K. A. Howard, and M. Godard (2013), Pervasive reactive melt migration through fast-spreading lower oceanic crust (Hess Deep, equatorial Pacific Ocean), *Earth Planet. Sci. Lett.*, *361*, 436–447.
Lonsdale, P. (1988), Structural pattern of the Galapagos microplate and evolution of the Galapagos Triple Junctions, *J. Geophys. Res.*, *93*, 13,551–13,574, doi:10.1029/JB093iB11p13551.
Luyendyk, B. P., and R. Day (1982), Paleomagnetism of the Samail Ophiolite, Oman. 2. The Wadi Kadir gabbro section, *J. Geophys. Res.*, *87*, 10,903–10,917, doi:10.1029/JB087iB13p10903.

MacLeod, C. J., B. Célérier, G. L. Früh-Green, and C. E. Manning (1996), Tectonics of Hess Deep: a synthesis of drilling results from Leg 147, in *Proc. ODP, Sci. Results*, vol. 147, edited by C. Mével et al., pp. 461–475, Ocean Drilling Program, College Station, Tex., doi:10.2973/odp.proc.sr.147.032.1996.

MacLeod, C. J., D. A. H. Teagle, K. M. Gillis, D. J. Shillington, and JC21 Scientific Party (2008), Morphotectonics of Hess Deep: Preliminary results of RRS *James Cook* Cruise JC21, *AGU abstract, 2008AGUAGUFM.V43I.08M*.

MacLeod, C. J., R. C. Searle, B. J. Murton, J. F. Casey, C. Mallows, S. C. Unsworth, K. L. Achenbach, and M. Harris (2009), Life cycle of oceanic core complexes, *Earth Planet. Sci. Lett.*, *287*, 333–344.

MacLeod, C., et al. (2002), Direct geological evidence for oceanic detachment fauling: The mid-Atlantic Ridge, 15°45′N, *Geology*, *30*, 279–282.

Maffione, M., A. Morris, O. Pluemper, and D. J. J. van Hinsbergen (2014), Magnetic properties of variably serpentinized peridotites and their implication for the evolution of oceanic core complexes, *Geochem. Geophys. Geosyst.*, *15*, 923–944, doi:10.1002/2013GC004993.

Mallows, C., and R. C. Searle (2012), A geophysical study of oceanic core complexes and surrounding terrain, mid-Atlantic Ridge 13°N–14°N, *Geochem. Geophys. Geosyst.*, *13*, Q0AG08, doi:10.1029/2012GC004075.

Malvoisin, B., J. Carlut, and F. Brunet (2012a), Serpentinization of oceanic peridotites: A high-sensitivity method to monitor magnetite production in hydrothermal experiments, *J. Geophys. Res.*, *117*, B01104, doi:10.1029/2011J008612.

Malvoisin, B., F. Brunet, J. Carlut, S. Rouméjon, and M. Cannat (2012b), Serpentinization of oceanic peridotites: Kinetics and processes of San Carlos olivine hydrothermal alteration, *J. Geophys. Res.*, *117*, B04102, doi:10.1029/2011JB008842.

Maus, S., et al. (2009), EMAG2: A 2′ resolution Earth magnetic anomaly grid compiled from satellite, airborne, and marine magnetic measurements, *Geochem. Geophys. Geosyst.*, *10*, Q08005, doi:10.1029/2009GC002471.

Mével, C., and C. Stamoudi (1996), Hydrothermal alteration of the upper mantle section at Hess Deep, in *Proc. ODP, Sci. Results*, vol. 147, edited by C. Mével et al., pp. 293–309, Ocean Drilling Program, College Station, Tex., doi:10.2973/odp.proc.sr.147.017.1996

Mitchell, N., M. Tivey, and P. Gente (2000), Seafloor slopes at midocean ridges from submersible observations and implications for interpreting geology from seafloor topography, *Earth Planet. Sci. Lett.*, *183*, 543–555.

Morris, A., J. S. Gee, N. Pressling, B. E. John, C. J. MacLeod, C. B. Grimes, and R. C. Searle (2009), Footwall rotation in an oceanic core complex quantified using reorientated Integrated Ocean Drilling Program core samples, *Earth Planet. Sci. Lett.*, *287*, 217–228.

Onwumechilli, A. (1967), Geomagnetic variations in the equatorial zone, in *Physics of Geomagnetic Phenomena*, edited by S. Matsushita and W. H. Campbell, pp. 426–507, Academic Press, San Diego, Calif.

Oufi, O., M. Cannat, and H. Horen (2002), Magnetic properties of variably sepentinized abyssal peridotites, *J. Geophys. Res.*, *107*(B5), 2095, doi:10.1029/2001JB000549.

Pariso, J. E., and H. P. Johnson (1991), Alteration processes at deep-sea drilling project/ocean drilling program Hole 504B at the Costa Rica rift: Implications for magnetization of oceanic crust, *J. Geophys. Res.*, *96*, 11,703–11,722, doi:10.1029/91JB00872.

Pariso, J. E., and H. P. Johnson (1993), Do lower crustal rocks record reversals of the Earth's magnetic field?: Magnetic petrology of oceanic Gabbros from Ocean Drilling Program Hole 735B, *J. Geophys. Res.*, *98*, 16,013–16,032, doi:10.1029/93JB00933.

Pariso, J. E., P. Kelso, and C. Richter (1996), Paleomagnetism and rock magnetic properties of gabbro from Hole 894G, Hess Deep, in *Proc. Ocean Dril. Prog. Sci. Res*, vol. 147, edited by C. G. Mével et al., pp. 373–381.

Parker, R. L., and S. P. Huestis (1974), The inversion of magnetic anomalies in the presence of topography, *J. Geophys. Res.*, *79*, 1587–1593, doi:10.1029/JB079i011p01587.

Phipps Morgan, J., and Y. J. Chen (1993), The genesis of oceanic crust magma injection, hydrothermal circulation, and crustal flow, *J. Geophys. Res.*, *98*, 6283–6297, doi:10.1029/92JB02650.

Raff, A. D. (1968), Seafloor spreading: Another rift, *J. Geophys. Res.*, *73*, 3699–3705, doi:10.1029/JB073i012p03699.

Richmond, R. M., R. A. Pockalny, J. W. King, R. L. Larson, and C. T. Popham (2004), Magnetic properties of ocean crust from the walls of Endeavor Deep: Implications for the source layers of marine magnetic anomalies, AGU Fall Meeting, Abstract T13B-1356.

Rioux, M., C. J. Lissenberg, N. M. McLean, S. A. Bowring, C. J. MacLeod, E. Hellebrand, and N. Shimizu (2012), Protracted time scales of lower crustal growth at the fast-spreading East Pacific Rise, *Nat. Geosci.*, NGEO01378, 1–4.

Russell, S. M., and R. B. Whitmarsh (2003), Magmatism at the west Iberia nonvolcanic rifted continental margin: Evidence from analyses of magnetic anomalies, *Geophys. J. Int.*, *154*(3), 706–730.

Saad, A. H. (1969), Paleomagnetism of Franciscan ultramafic rocks from Red Mountain, California, *J. Geophys. Res.*, *74*, 6567–6578, doi:10.1029/JB074i027p06567.

Sato, T., K. Okino, and H. Kumagai (2009), Magnetic structure of an oceanic core complex at the southernmost Central Indian Ridge: Analysis of shipboard and deep-sea three-component magnetometer data, *Geochem. Geophys. Geosyst.*, *10*, Q06003, doi:10.1029/2008GC002267.

Schouten, H., D. K. Smith, L. G. J. Montési, W. Zhu, and E. M. Klein (2008), Cracking north of the Galápagos triple junction, *Geology*, *36*, 339–342.

Seama, Y., Y. Nogi, and A. Isezaki (1993), A new method for precise determination of the position and strike of magnetic boundaries using vector data of the geomagnetic anomaly field, *Geophys. J. Int.*, *113*, 155–164.

Smith, D. K., J. R. Cann, and J. Escartin (2006), Widespread active detachment faulting and core complex formation near 13°N on the mid-Atlantic Ridge, *Nature*, *442*, 440–443.

Smith, D. K., J. Escartin, H. Schouten, and J. R. Cann (2008), Fault rotation and core complex formation: Significant processes in seafloor formation at slow-spreading midocean ridges (mid-Atlantic Ridge, 13′–15°N), *Geochem. Geophys. Geosyst.*, *9*, Q03003, doi:10.1029/2007GC001699.

Smith, D. K., H. Schouten, W. Zhu, and L. Montesi (2013), The recent history of the Galapagos Triple Junction preserved on the Pacific plate, *Earth Planet. Sci. Lett.*, *371–372*, 6–15, doi:10.1016/j.epsl.2013.04.018.

Spector, A., and F. S. Grant (1970), Statistical models for interpreting aeromagnetic data, *Geophysics*, *35*, 293–302.

Szitkar, F., J. Dyment, Y. Fouquet, Y. Choi, and C. Honsho (2015), Absolute magnetization of the seafloor at a basalt-hosted hydrothermal site: Insights from a deep-sea submersible survey, *Geophys. Res. Lett.*, *42*, 1046–1052, doi:10.1002/2014GL062791.

Talwani, M., and J. R. Heirtzler (1964), Computation of magnetic anomalies caused by two-dimensional structures of arbitrary shape, in *Computers in the Mineral Industries*, edited by G. A. Parks, pp. 464–480, Stanford Univ. Press, Stanford, Calif.

Tivey, M. A. (1996), The vertical magnetic structure of ocean crust determined from near-bottom magnetic field measurements, *J. Geophys. Res.*, *101*, 20,275–20,296, doi:10.1029/96JB01307.

Tivey, M. A., and G. L. Christeson (1999), High-resolution magnetic imaging of extrusive and intrusive crust at Hess Deep and a comparison with Juan de Fuca and Hole 504B results, *Eos Trans. AGU*, *80*, F985.

Tivey, M. A., and B. E. Tucholke (1998), Magnetization of 0–29 Ma ocean crust on the mid-Atlantic Ridge, 25′30 to 27′10°N, *J. Geophys. Res.*, *103*, 17,807–17,826, doi:10.1029/98JB01394.

Tivey, M. A., H. P. Johnson, M. S. Salmi, and M. Hutnak (2014), High-resolution near-bottom vector magnetic anomalies over Raven Hydrothermal Field, Endeavour Segment, Juan de Fuca Ridge, *J. Geophys. Res. Solid Earth*, *119*, 7389–7403.

Tominaga, M., and W. W. Sager (2010), Origin of the smooth zone in early Cretaceous North Atlantic magnetic anomalies, *Geophys. Res. Lett.*, *37*, L01304, doi:10.1029/2009GL040984.

Tucholke, B. E., J. Lin, and M. C. Kleinrock (1998), Megamullions and mullion structure defining oceanic metamorphic core complexes on the mid-Atlantic Ridge, *J. Geophys. Res.*, *103*, 9857–9866, doi:10.1029/98JB00167.

Varga, R. J., J. A. Karson, and J. S. Gee (2004), Paleomagnetic constraints on deformation models for uppermost oceanic crust exposed at the Hess Deep Rift: Implications for axial processes at the East pacific Rise, *J. Geophys. Res.*, *109*, B02104, doi:10.1029/2003JB002486.

Vine, F. J., and D. H. Matthews (1963), Magnetic anomalies over oceanic ridges, *Nature*, *199*, 947–949.

Wessel, P. (1989), XOVER: A Cross-over Error Detector for Track Data, *Comput. Geosci.*, *15*, 333–346.

Wessel, P. (2010), Tools for analyzing intersecting tracks: The x2sys package, *Comput. Geosci.*, *36*, 348–354.

Wiggins, S. M., L. M. Dorman, B. D. Cornuelle, and J. A. Hildebrand (1996), Hess Deep rift valley structure from seismic tomography, *J. Geophys. Res.*, *101*, 22,335–22,353, doi:10.1029/96JB01230.

Wilson, D. S., and R. N. Hey (1981), The Galapagos axial magnetic anomaly: Evidence for the Emperor event within the Brunhes and for a two-layer magnetic source, *Geophys. Res. Lett.*, *8*, 1051–1054, doi:10.1029/GL008i010p01051.

Zhao, X., and M. Tominaga (2009), Paleomagnetic and rock magnetic results from lower crustal rocks of IODP Site U1309: Implication for thermal and accretion history of the Atlantic Massif, *Tectonophysics*, doi:10.1016/j.tecto.2009.04.017.